Dramatic promotion of visible-light photoreactivity of TiO$_2$ hollow microspheres towards NO oxidation by introduction of oxygen vacancy

Zhao Hu[a], Kaining Li[a], Xiaofeng Wu[a], Ning Wang[b,*], Xiaofang Li[c], Qin Li[a], Lin Li[a], Kangle Lv[a,*]

[a] College of Resources and Environmental Science, South-Central University for Nationalities, Wuhan, 430074, PR China
[b] Advanced Membranes and Porous Materials Center, Physical Sciences and Engineering Division, King Abdullah University of Science and Technology (KAUST), Thuwal, 23955-6900, Saudi Arabia
[c] College of Chemistry and Chemical Engineering, Wuhan University of Science and Technology, Wuhan, 430081, PR China

ARTICLE INFO

ABSTRACT

Hollow-structured TiO$_2$ has attracted much attention owing to its low density, good light-reflecting ability, and excellent permeability. However, the wide bandgap (about 3.2 eV for anatase TiO$_2$) and fast recombination of photo-generated carriers hamper its practical application. Herein, oxygen vacancy (O$_V$) was introduced onto the surface of TiO$_2$ hollow microspheres (TiO$_2$-HMSs) by a facile method through calcination of the mixture of hydrogen titanate hollow microspheres (H$_2$TiO$_3$-HMSs) and urea. Using this strategy, both the aims of extending the light-response range and promoting the separation of photo-generated carriers were satisfactorily achieved. The introduction of Ov facilitates the adsorption and activation of NO and O$_2$ on the surface of TiO$_2$-HMSs. This stimulates the production of reactive oxygen species, such as superoxide radicals ($^{\cdot}O_2^-$) and hydroxyl radicals ($^{\cdot}OH$), resulting in the dramatic promotion of visible-light photocatalytic oxidation of NO.

1. Introduction

Semiconductor photocatalysis has aroused significant interest because it is a promising approach to address the problems of energy crisis and environmental pollution [1,2]. Applications of photocatalysis include water splitting to produce hydrogen [3–6], dye-sensitized solar cells [7], sterilization [8], and degradation of organic pollutants in water [9–15] and air [15]. Among the typical photocatalytic semiconductor materials, TiO$_2$ is the most studied because of its strong oxidizing power, chemical inertness, and excellent biocompatibility [16]. Recently, much attention has been paid to hollow-structured TiO$_2$ materials, particularly TiO$_2$ hollow microspheres (TiO$_2$-HMSs), because they have the merits of low density, good permeability, and ease of recycling — qualities that make them good candidates for air purification [17,18]. However, the wide band gap (3.2 eV for anatase TiO$_2$) and fast recombination of photo-generated carriers in pristine TiO$_2$ results in poor utilization of solar light and low quantum efficiency, which hamper the practical application of TiO$_2$. To address these limitations, many strategies have been used to modify TiO$_2$, such as doping [19], noble metal deposition [20], semiconductor coupling [21], and exposure of high energy facets [22].

Black TiO$_2$ with surface oxygen vacancy (Ov) has been prepared by hydrogenation of TiO$_2$ nanoparticles under high-temperature and high-

pressure conditions [23]. Although this material exhibits a broad range of visible-light response and improved hydrogen production rate, the synthetic method is not so good because it is time-consuming and requires special instrumentation as it may cause explosion. A strategy based on fast-reducing flame treatment to introduce Ov to nickel-iron layered double hydroxides was recently reported [24]. However, this treatment is sensitive to the location of the sample in the flame, and it is very difficult to precisely control the concentration of Ov. Bismuth oxychloride (BiOCl) with Ov has been prepared by microwave-assisted heating of a mixture of BiOCl and a surfactant, ethylene glycol [25]. Considering the strong adsorption of surfactant on the surface of BiOCl, it is reasonable to deduce that the surface with Ov is easily polluted by the surfactant. Therefore, the development of a safe and easy method to prepare a surface-clean semiconductor with Ov without the use of any sophisticated instrument is of great importance but remains a big challenge.

Herein, we proposed a facile method to prepare TiO$_2$-HMSs with Ov (Ov-TiO$_2$-HMSs) and applied it to the photocatalytic oxidation of NO (see Fig. S1 for set-up). Ov-TiO$_2$-HMSs was prepared by calcination of a mixture of titanate HMSs (H$_2$TiO$_3$-HMSs) and urea in a Muffle furnace at 600 °C for only 2 h. During the phase transformation of H$_2$TiO$_3$-HMSs to anatase TiO$_2$-HMSs at high temperature, the oxidation of urea creates an oxygen-deficient environment in the crucible that favors the

---

formation of oxygen vacancy on the surface of anatase TiO_2-HMSs. The introduction of Ov not only improved the visible photoreactivity by enhanced adsorption and activation, but also affected the photocatalytic oxidation pathway of NO. This method has the merits of simplicity, safety, and ease of scale-up for production without the use of any special instruments. Control experimental result showed that graphitic carbon nitride (g-C_3N_4) was obtained by direct polymerization of urea at 600 °C for 2 h, which is consistent with the literature [26].

2. Experimental

2.1. Preparation of Ov-TiO$_2$-HMSs

To obtain Ov-TiO_2-HMSs with large BET surface areas, we first prepared hydrogen titantate hollow microspheres assembly from nanosheets (H_2TiO_3-HMSs-NSs) according to our previous work [7,27], and the detailed procedures can be seen from the supporting information. The obtained H_2TiO_3-HMSs powder (2.0 g) was then mixed with varying amounts of urea (1.0, 2.0, 4.0, and 6.0 g). Note that the crucible is almost full when the amount of urea is 6.0 g. Therefore, the urea used in the present study is no more than 6.0 g. The mixture was transferred to a 50-ml crucible, which was then calcined in a Muffle furnace at 600 °C for 2 h at a heating rate of 5 °C min^{-1}. The prepared Ov-TiO_2-HMSs samples were denoted as Ux (U1, U2, U4, and U6), where x represents the amount of urea in the mixture before calcination. For comparison, a TiO_2-HMSs sample without urea (U0) was also prepared by direct calcination of 2.0 g of H_2TiO_3-HMSs powder under other identical conditions.

2.2. Characterization

The phase structure of the photocatalyst was determined using the D8 Advance X-ray diffractometer (Bruker, Germany). The morphology of the photocatalyst was observed through the Tecnai G20 field-emission transmission electron microscope (FEI Co., USA) and S-4800 field-emission scanning electron microscope (Hitachi, Japan). The Brunauer-Emmett-Teller (BET) surface area and pore structure of the photocatalyst were measured on the ASAP 2020 nitrogen adsorption apparatus (Micromeritic Instruments, USA). All samples were degassed at 160 °C prior to BET measurements. The UV–vis diffuse reflectance spectra were obtained using the LambdaBio35 UV–vis spectrophotometer (PerkinElmer, Inc., USA) with $BaSO_4$ as the reference. Fourier-transform infrared spectra were recorded on the NEXUIS-470 infrared spectrometer (Nicolet Co., USA). The electron paramagnetic resonance (EPR) signal was recorded on the Bruker EMX EPR spectrometer (Bruker, USA). Photoluminescence (PL) and time-resolved fluorescence emission spectra were measured on the FLSP-920 fluorescence spectrophotometer (Edinburgh Instruments, UK). The surface photovoltage response was measured on a homemade, multi-functional photoelectric spectrometer.

2.3. (Photo)electrochemical measurement

The photocurrent and electrochemical impedance were measured on a three-electrode system in an electrochemical workstation (CHI760E, Shanghai, China). For the photocurrent measurement, 20 mg of the photocatalyst was dispersed in 1 ml of a 1:1 (v/v) mixture of ethanol and water, which was then ultrasonicated for 30 min and followed by the addition of 30 μl of naphthol to form the gel. The indium-tin oxide/TiO_2 electrode was prepared via the doctor-blade method. Na_2SO_4 (0.4 mol·L^{-1}) was used as the electrolyte, and a 3-W LED lamp that emitted mainly at λ = 420 ± 10 nm was used as the light source. Electrochemical impedance was measured under open-circuit potential with a frequency between 0.1 and ~1000 Hz.

2.4. Radical trapping

The electron spin resonance (ESR) signals of the radicals that were spin-trapped by 5,5-dimethyl-1-pyrroline *N*-oxide (DMPO) were recorded on the JES FA200 spectrometer (JEOL, Japan). Specimens for the ESR measurement were prepared by mixing the photocatalyst with 40 mM DMPO solution in a beaker (methanol dispersion for DMPO-O_2•– and aqueous dispersion for DMPO-HO•) and illuminating it with visible light (λ > 400 nm).

2.5. Density functional theory (DFT) calculations

All spin-polarized DFT-D2 calculations were conducted using the Vienna Ab initio Simulation Package (VASP code 5.4.1). The generalized gradient approximation was used as the exchange-correlation functional [28]. The cut-off energy and Gaussian trailing width were set to 400 and 0.2 eV, respectively, while the K-points were $2 \times 2 \times 2$. All geometries and energies were converged to below 0.01 eV. The Heyd-Scuseria-Ernzerhof (HSE06) method was used to estimate the energy band structure and state density. The $3 \times 3 \times 1$ supercell model containing 108 atoms with the (101) crystal plane exposed was adopted to simulate pristine TiO_2-HMSs (designated simply as pristine TiO_2). Ov-TiO_2-HMSs (designated simply as Ov-TiO_2) was simulated by removing one oxygen atom in the supercell. The adsorption energy E_{ads} is defined as $E_{ads} = E_{tot} - E_T - E_{mol}$, where E_{tot}, E_T and E_{mol} denote the total energy of the compounds, adsorbent (pristine TiO_2 or Ov-TiO_2), and adsorbed molecules after adsorption, respectively.

2.6. Photocatalytic oxidation of NO

Photocatalytic NO oxidation was performed in a continuous-flow reactor (see Fig. S1). Firstly, 200 mg of TiO_2 photocatalyst powder was dispersed in 30 ml of water and sonicated for 10 min. The resulting suspension was then transferred to a culture dish, with a diameter of about 11.5 cm, and dried in an electronic oven at 80 °C for 3 h. After cooling down to room temperature, the dish with the TiO_2 photocatalyst film was placed in the reaction chamber. NO gas was supplied from a compressed gas cylinder having 50 ppm of NO (N_2 balance) in line with traceable standards recommended by the National Institute of Standards and Technology. Before irradiation, NO and air from the cylinders were mixed through the gas bottle (blender) and the humidity of the mixed gas is about 50%. The concentration of NO in the gas mixture was adjusted to about 600 ppb by employing mass flow controllers. After reaching the adsorption-desorption equilibrium of NO on the surface of the TiO_2 photocatalyst, a 30 W LED lamp (λ > 400 nm) was turned on to begin the NO photocatalytic oxidation. The Model T200 chemiluminescence NOx analyzer (Advanced Pollution Instrumentation, Teledyne Technologies, USA) was used to monitor the concentrations of NO and NO_2 at a gas flow rate of 1.0 L·min^{-1}.

3. Results and discussion

3.1. XRD and FT-IR

The corresponding X-ray diffraction (XRD) and Fourier-transform IR (FTIR) spectra of S_{pu} sample are shown in Fig. 1A and B, respectively, where the diffraction peak centering at 27° is indexed as the (002) peak that originates from the stacking of the conjugated aromatic system (Fig. 1A), and the vibrations between 1635–1250 cm^{-1} are attributed to the typical stretching modes of g-C_3N_4 heterocycles (Fig. 1B). This indicates that the component of S_{pu} sample is carbon nitrides (g-C_3N_4). As expected, direct calcination of H_2TiO_3-HMSs resulted in the formation of TiO_2-HMSs, which are identified as the pure anatase TiO_2 phase from the XRD and FTIR spectra. The sharp diffraction peak at 2θ = 25.3° corresponds to the (101) plane diffraction of anatase TiO_2, and the absorption peaks centering at about 1088 and 467 cm^{-1} originates
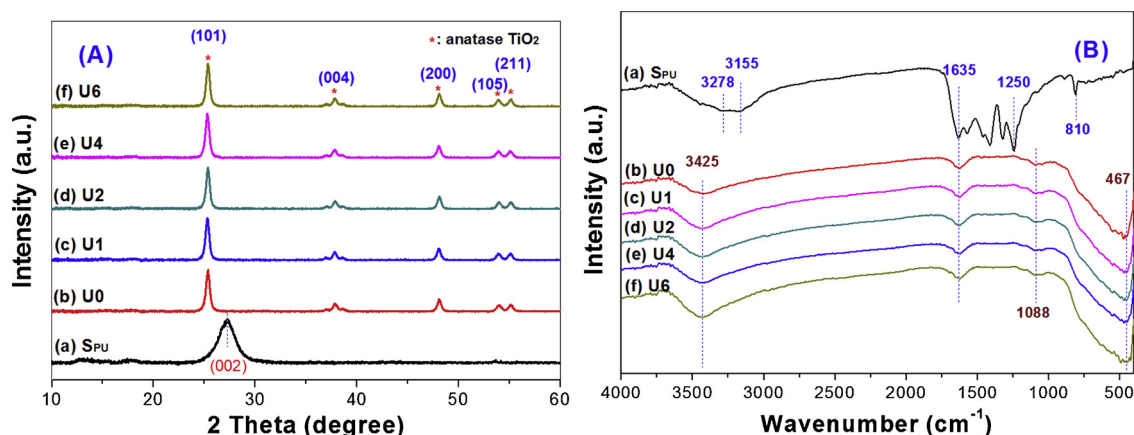
Fig. 1. XRD patterns (A) and FTIR spectra (B) of the photocatalysts. S_{PU} is g-C_3N_4, U0 is pristine TiO_2-HMSs, and Ux is Ov-TiO_2-HMSs prepared using x g of urea.
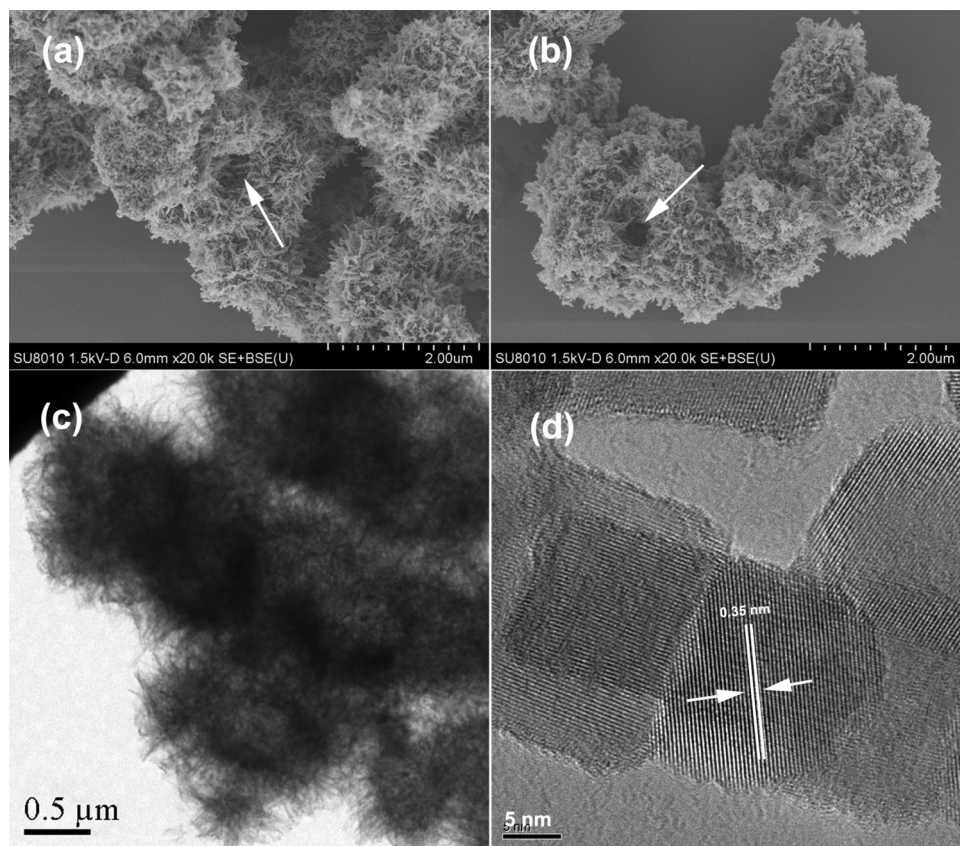

Fig. 2. SEM (a and b) and TEM (c) images of pristine TiO_2-HMSs (a for U0 sample) and Ov-TiO_2-HMSs (b and c for U6 sample). Arrows in images (a) and (b) indicate the observation of hollow structures of TiO_2-HMSs. (d) is the high resolution TEM image of Ov-TiO_2-HMSs for U6 sample.

from the vibrations of Ti-O and O-Ti-O, respectively. Unexpectedly, only anatase TiO_2 instead of the g-C_3N_4/TiO_2 hybrid was obtained by calcining the mixture of H_2TiO_3-HMSs and urea under other identical conditions, that is, no signals indicating the presence of g-C_3N_4 are observed in either the XRD or FTIR spectra of all Ov-TiO_2-HMSs samples.

Liu et al. has reported the successful introduction of Ov into WO_3 simply by calcination of WO_3 in NH_3 gas at 350 °C for 1 h without the introduction of N element [29]. According to the on-line gas mass spectrometry, N_2O, NO, N_2, H_2, and H_2O were detected during the temperature-programmed reaction of WO_3 with ammonia. Then they proposed that the production of Ov-WO_3 without N-doping is ascribed to the ammonia-assisted reduction strategy. As H and N atoms can extract O atoms in WO_3 to form H_2O and N_2O at low temperature, it is

not strange to obtain Ov-enriched WO_3 (Eq. (1)).

$$WO_3 + NH_3 \rightarrow WO_{3-x} + N_2O + H_2O \tag{1}$$
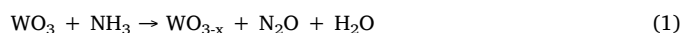
Similarly, in the present study, TiO_2-HMSs may catalyze the decomposition of urea to produce TiO_2-HMSs with Ov, preventing its polymerization to form g-C_3N_4. Then we can't obtain TiO_2-HMSs/g-C_3N_4 composite.

From the SEM images of pristine TiO_2-HMSs (Fig. 2a) and Ov-TiO_2-HMSs (Fig. 2b), we can see that both samples have similar morphology, reflecting that the presence of urea has little effects on the morphology of TiO_2-HMSs. The hollow structures of Ov-TiO_2-HMSs were further confirmed by the TEM image (Fig. 2c). The high resolution TEM image of the Ov-TiO_2-HMSs is shown in Fig. 2d, where the distinct fringes of
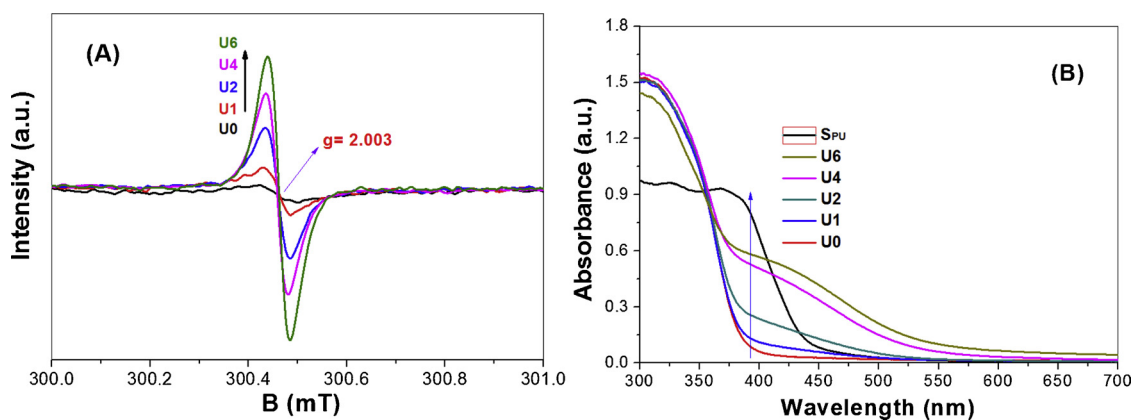
Fig. 3. EPR (A) and diffuse reflectance spectra (B) of the photocatalysts. U0 is pristine TiO_2-HMSs and Ux is Ov-TiO_2-HMSs prepared using x g of urea.
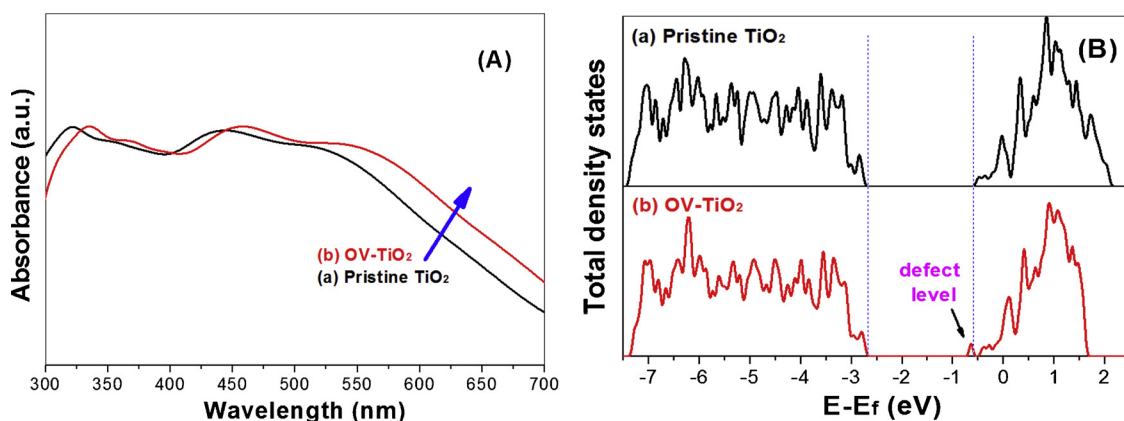

Fig. 4. Calculated UV–vis absorption spectra (A) and total density of states (DOS) (B) of TiO_2 before and after introduction of Ov. The Fermi level is set to 0 eV.
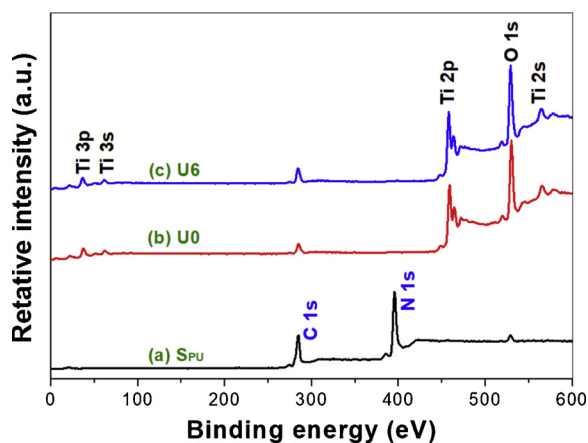

Fig. 5. XPS survey spectra of the photocatalysts.

d = 0.35 nm corresponds to the (101) crystallographic planes of anatase TiO_2 nanocrystals.

3.2. Electron paramagnetic resonance and diffuse reflectance spectra

The formation of Ov on the surface of TiO_2-HMSs is confirmed by the electron paramagnetic resonance (EPR) spectra of the samples, where the strong signal centering at g = 2.003 originates from the Ov-trapped electrons (Fig. 3A) [30–32]. The intensity of the signal steadily increases with increasing the amount of urea, which implies that adjusting this amount allows the concentration of Ov to be easily tailored to enable the study of the intrinsic role of Ov in photocatalytic

oxidation. Coincidentally, a long tail in the visible region can be observed in the UV–vis absorption spectrum of Ov-TiO_2-HMSs (Fig. 3B), which shifts to higher absorbance values with an increase in the amount of urea. This reflects the Ov-induced bandgap narrowing [33], which is consistent with the density functional theory (DFT)-calculated UV–vis absorption spectrum (Fig. 4A). Fig. 4B compares the total density of states (DOS) of pristine TiO_2 and Ov-TiO_2. The bandgap of Ov-TiO_2 is narrower than that of pristine TiO_2 owing to the formation of defect energy levels in the band gap. This is responsible for the greater visible-light absorption ability as secondary light absorption occurs, which can enhance the photocatalytic activity.

3.3. XPS analysis and photo(electro)chemical measurements

Fig. 5 shows the XPS spectra of the photocatalysts. It can be seen that S_{pu} sample only contains C and N, and a small amount of O, while both pristine TiO_2-HMSs and Ov-TiO_2-HMSs have similar XPS survey spectra. Comparison of their high-resolution XPS spectra in the Ti 2p (Fig. 6A) and O 1s (Fig. 6B) regions indicates that the introduction of Ov into TiO_2-HMSs results in decreased binding energies for both Ti and O. This is because two additional electrons are left once an oxygen atom is removed from the surface of TiO_2, causing increased electron cloud density around the Ti and O atoms near the Ov sites.

Fig. 6C compares the high resolution XPS spectra in C 1s region between U0 and U6 sample, which can be deconvoluted into three peaks with binding energies of 284.6, 286.6 and 288.4 eV, respectively. The main peak with binding energy of 284.6 eV is ascribed to the adventitious hydrocarbon from the XPS instrument itself [34], while the peaks with binding energies of 286.6 and 288.4 eV are attributed to oxidized carbon species with C–O and C=O bonds [35]. As there is no obvious peak with a binding energy of about 282.0 eV which
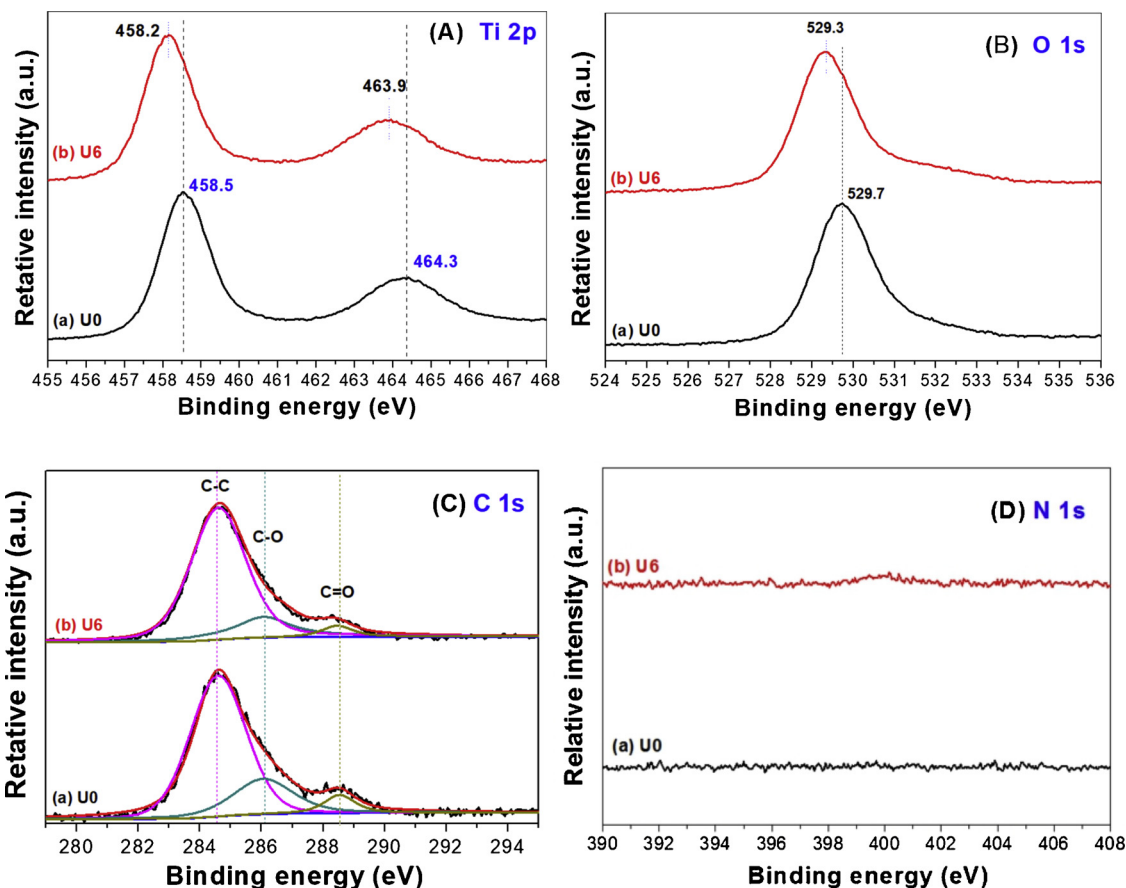
Fig. 6. High-resolution XPS spectra in the Ti 2p (A), O 1s (B), C 1s (C) and N 1s (D) regions. S_{PU} is g-C_3N_4, U0 is pristine TiO_2-HMSs, and U6 is Ov-TiO_2-HMSs.
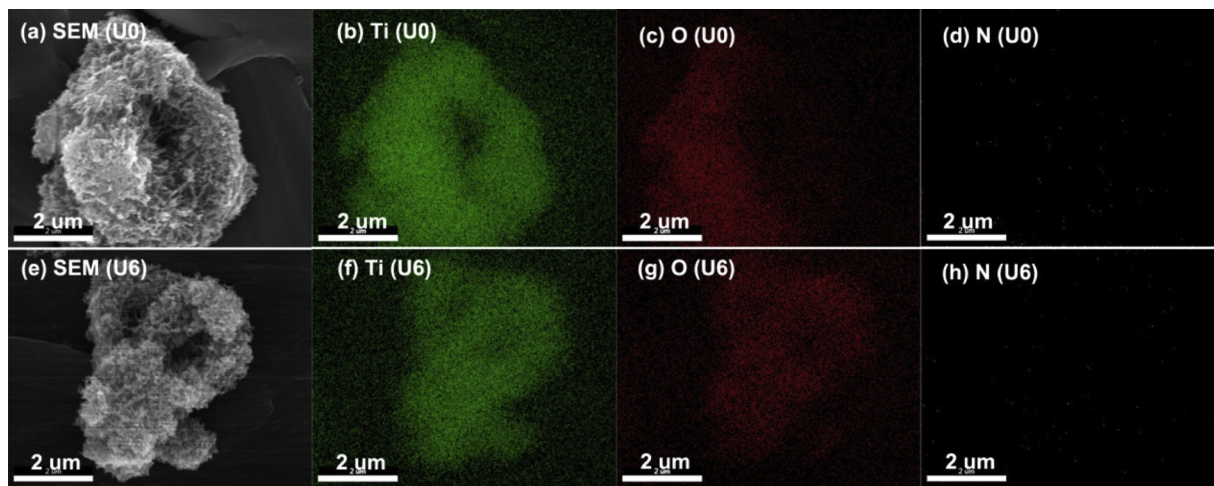

Fig. 7. EDX mapping of U0 (a–d) and U6 (e–h) samples.

corresponds to Ti−C bond can be observed from both samples, we can conclude that C element is not doped into the lattice of Ov-TiO_2-HMSs [36]. The high-resolution XPS spectrum in the N 1s region (Fig. 6D) shows that the N signal for Ov-TiO_2-HMSs is very weak, which also implies that N doping of the Ov-TiO_2-HMSs lattice can be ruled out.

As the high resolution XPS spectra of pristine TiO_2-HMSs and Ov-TiO_2-HMSs in C1s and N 1s regions are similiar, the stronger UV–vis absorption of Ov-TiO_2-HMSs should be caused by surface oxygen vacancy instead of the doping of C and N elements.

Fig. 7 shows the EDX mapping of TiO_2-HMSs for U0 and U6 samples. From the elemental maps, we can clearly observe the homogeneous distribution of Ti and O elements over TiO_2-HMSs. On the contrary, as the N element is almost undetectable for both samples, the possibility for the doping of N into the lattice of TiO_2-HMSs during calcination can be excluded, which is consistent with the XPS characterization results (Fig. 6D).

Fig. 8A compares the photocurrents of g-C_3N_4 (Spu), pristine TiO_2-HMSs (U0) and Ov-TiO_2-HMSs (U6) samples. It can be seen that the photocurrent of g-C_3N_4 is only $0.85\,\mu A\cdot cm^{-2}$, which increases to $2.7\,\mu A\cdot cm^{-2}$ for TiO_2-HMSs and then to $8.5\,\mu A\cdot cm^{-2}$ for Ov-TiO_2-HMSs. Careful view shows that the shapes of the photocurrents for g-C_3N_4 and Ov-TiO_2-HMSs are totally different. The photocurrent of g-C_3N_4
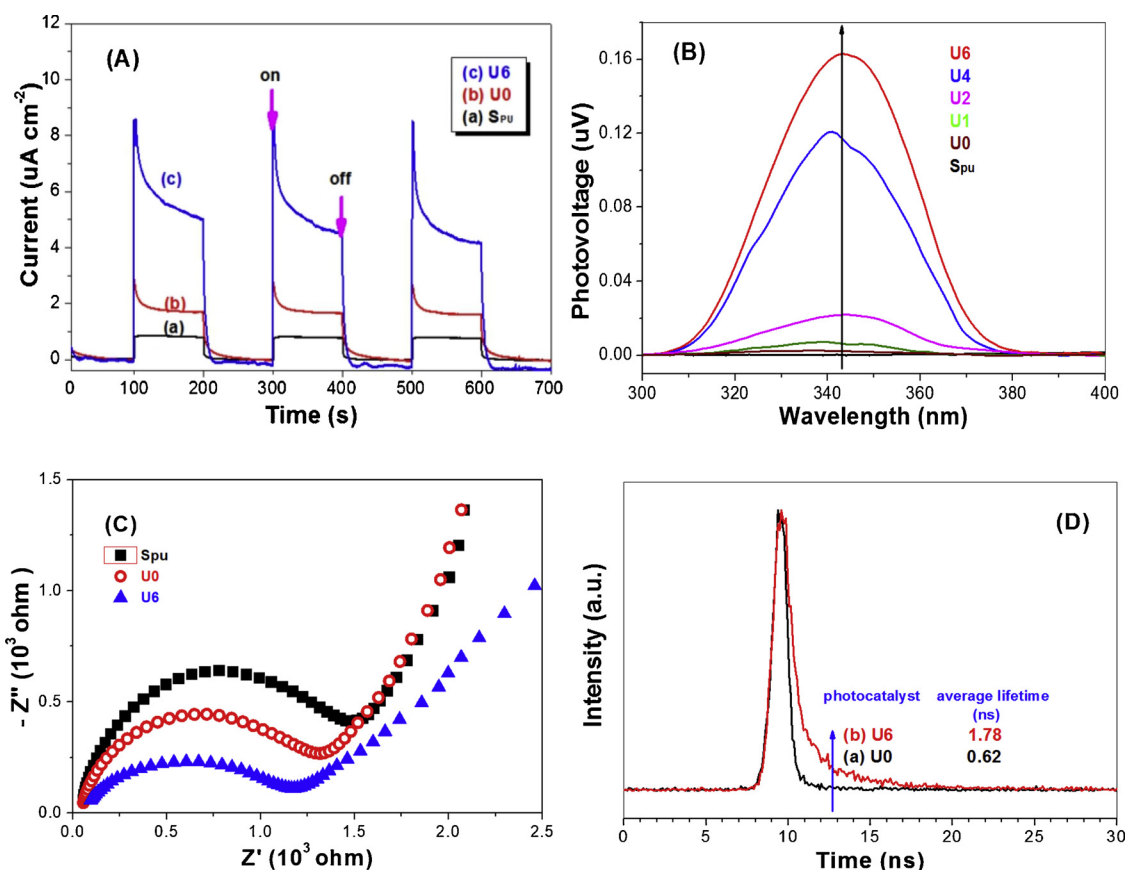
Fig. 8. Photocurrents (A), surface photovoltage spectra (B), electrochemical impedance spectroscopy (EIS) Nyquist plots (C), and time-resolved photoluminescence decay spectra (D) of the photocatalysts. S_{PU} is g-C_3N_4, U0 is pristine TiO_2-HMSs, and Ux is Ov-TiO_2-HMSs prepared using x g of urea.
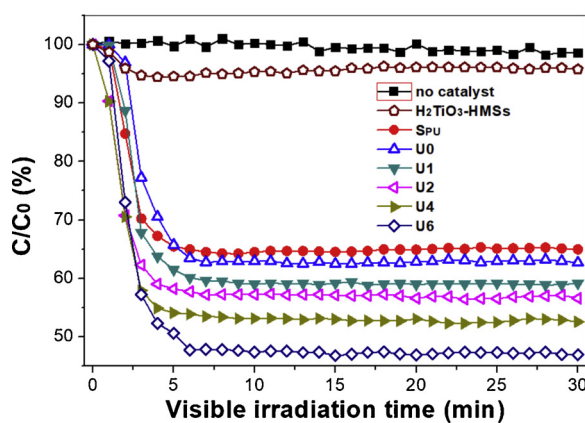

Fig. 9. Photocatalytic oxidation curves for NO oxidation on different photo-catalysts. S_{PU} is g-C_3N_4, U0 is pristine TiO_2-HMSs, and Ux is Ov-TiO_2-HMSs prepared using x g of urea.

Fig. 10. Nitrogen adsorption-desorption isotherms of the photocatalysts and the corresponding pore size distribution curves (inset). S_{PU} is g-C_3N_4, U0 is pristine TiO_2-HMSs, and U6 is Ov-TiO_2-HMSs.

increases smoothly before levelling off upon illumination, indicating that almost all the photo-generated holes are injected to the electrolyte. However, no steady Faradaic current, but an obvious anodic photo-current spike is observed on illuminated Ov-TiO_2-HMSs electrode. This reflects that there are photo-generated holes accumulated at the electrode/electrolyte interface instead of injection to the electrolyte for illuminated Ov-TiO_2-HMSs electrode, which is possibly due to the instant production of high concentrated holes. The intensity of the spiky photocurrent for Ov-TiO_2-HMSs (U6) is much stronger than that of pristine TiO_2-HMSs (U0), which infers that the separation of photo-generated electron-hole pairs over illuminated Ov-TiO_2-HMSs is more efficient than over pristine TiO_2-HMSs. The accumulated positive holes of Ov-

TiO_2-HMSs at the electrode/electrolyte interface then can prevent the further migration of negative electrons to photocathode due to the electrostatic interaction, which therefore results in a reduced photo-current. So it is not strange to observe that the photocurrent of Ov-TiO_2-HMSs sharply increases and then begins to slowly decrease upon irradiation.

Consistent with the result of photocurrent, the improved separation of photo-generated carriers of Ov-TiO_2-HMSs is also observed from the increased surface photovoltage as shown in Fig. 8B, from which it can be clearly seen that U6 sample exhibits the highest surface photovoltage among all the photocatalysts.

When compared with that of pristine TiO_2-HMSs, the arc radius of

Table 1
Physical properties of the photocatalysts.

Sample	Starting materials		Component	Relative crystallinity[a] (nm)	Nitrogen sorption		
	TiO$_2$ (g)	Urea (g)			SA$_{BET}$[b] (m$^2 \cdot$g^{-1})	PV[c] (cm$^3 \cdot$g^{-1})	APS[d] (nm)
U0	2.0	0	pristine TiO$_2$	1.00	79.6	0.61	13.8
U1	2.0	1.0	O$_V$-TiO$_2$	1.01	77.7	0.57	14.0
U2	2.0	2.0	O$_V$-TiO$_2$	0.99	66.4	0.50	13.8
U4	2.0	4.0	O$_V$-TiO$_2$	1.06	61.8	0.50	16.1
U6	2.0	6.0	O$_V$-TiO$_2$	1.03	67.4	0.58	17.2
S$_{PU}$	0	6.0	g-C$_3$N$_4$	–	71.9	0.37	11.8

[a] Relative crystallinity of TiO$_2$ is evaluated via the relative intensity of anatase (101) plane diffraction peak using U0 as reference.
[b] Brunauer-Emmett-Teller (BET) surface area (SA) is determined by the multipoint BET method using the adsorption data in the relative pressure (P/P_0) range from 0.05 to 0.3.
[c] Pore volume (PV) is determined from the adsorption branch of the nitrogen isotherms at $P/P_0 = 0.994$.
[d] Average pore size (APS) is estimated from the adsorption branch of the nitrogen isotherms using the Barrett-Joyner-Halenda method.
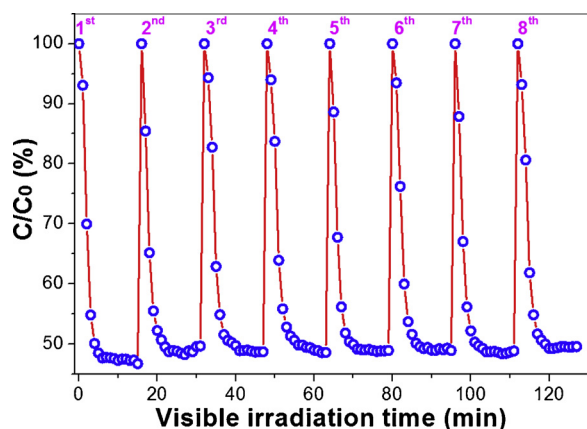

Fig. 11. Photocatalytic oxidation curve for recycling test of Ov-TiO$_2$-HMSs (U6 sample).
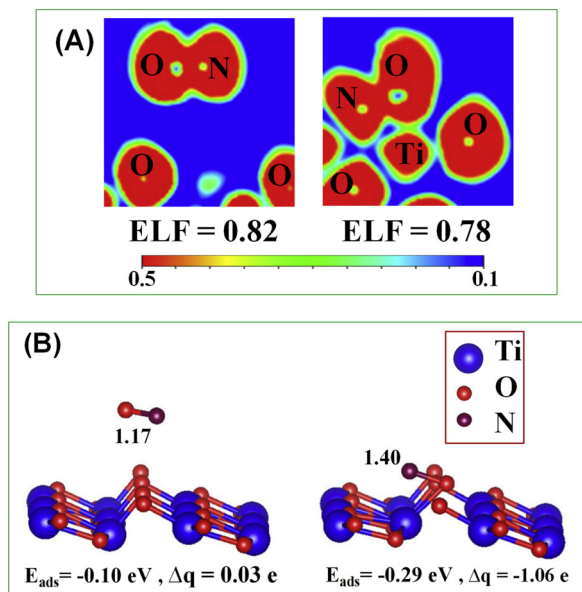

Fig. 12. Comparison of the electronic local functions (ELF) (A) and optimized structural models (B) of pristine TiO$_2$ and Ov-TiO$_2$ after adsorption of NO. E_{ads} is the adsorption energy and Δq is the Bader charge.

Ov-TiO$_2$-HMSs on the Nyquist plot in the high frequency range of the electrochemical impedance spectroscopy data is much smaller (Fig. 8C), suggesting the quicker interfacial charge transfer to the

electron donor/acceptor of Ov-TiO$_2$-HMSs (U6) than pristine TiO$_2$-HMSs (U0).

The intensity of photoluminescence (PL) spectrum of TiO$_2$-HMSs steadily decreases with an increase in the concentration of Ov, reflecting the retardation of carrier recombination by Ov (see Fig. S2). According to the transient PL spectra shown in Fig. 8D, the average lifetime of TiO$_2$-HMSs nearly increases three-fold (from 0.62 to 1.78 ns) after the introduction of Ov (Fig. 8D). These results suggest that Ov-induced localized states not only could extend the light-response range, but also facilitate the trapping of charge carriers, which therefore can enhance the photocatalytic activity.

A fully oxidized surface interacts weakly with O$_2$ and NO, which is unfavorable for NO oxidation. Surface Ov not only changes the coordination number of the lattice Ti, but also lengthens the distance between the neighboring titanium atoms (Ti3 and Ti4) from 2.83 to 3.36 nm (see Fig. S3). Such large lattice distortion would cause dipole distance changes, which result in a built-in electric field and consequently promote the effective separation of photo-generated electron-hole pairs [31].

3.4. Visible photocatalytic oxidation of NO

As a typical pollutant from vehicle exhaust, the presence of NO in air is of increasing environmental concern because NO is the major contributor to acid rain and urban smog. Long-time exposure to NO-contaminated air can also cause serious respiratory diseases [37]. Therefore, NO oxidation was used to measure the photocatalytic activity of TiO$_2$-HMSs, which was performed in a continuous-flow reactor under irradiation of a visible-light LED lamp equipped with a cutoff filter ($\lambda > 400$ nm) to remove UV light. The set-up of the NO oxidation experiment is illustrated in Fig. S1 [35]. From Fig. 9, we can clearly see that the concentration of NO from the outlet of the reactor begins to decrease after turning on the LED lamp, reflecting that TiO$_2$-HMSs is photoreactive toward NO oxidation. It can also be seen that NO is very stable under the irradiation of LED lamp, and the precursor of TiO$_2$-HMSs before calcination exhibits very poor NO oxidation activity because it is titanate (H$_2$TiO$_3$). After calcination, the resulting anatase TiO$_2$-HMSs shows evident NO oxidation activity (37.5% removal rate), which steadily increases with increasing concentration of Ov. The NO removal rate soars to 53.2% using Ov-TiO$_2$-HMSs of U6 as photocatalyst, an improvement by a factor of 1.42.

On considering that BET surface area of the photocatalyst plays an important role on its photoreactivity, we measured the nitrogen sorption isotherms of the photocatalysts. Fig. 10 compares the nitrogen sorption isotherms of g-C$_3$N$_4$, pristine TiO$_2$-HMSs (U0), and Ov-TiO$_2$-HMSs (U6). The adsorption isotherms of the three samples almost overlap in the relative pressure range of 0.05–0.3, reflecting the similar BET surface areas of the photocatalysts. Since the BET surface areas of
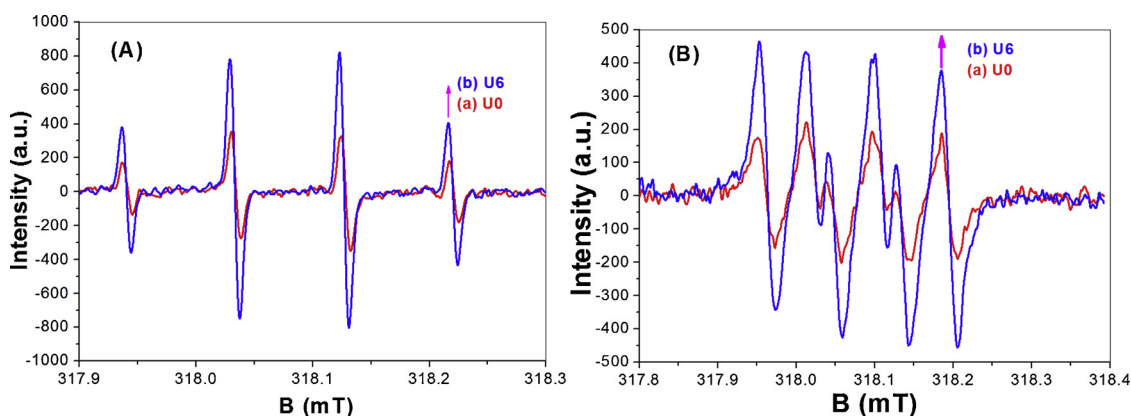
Fig. 13. ESR signals of DMPO-HO• (A) and DMPO-O$_2$•– (B) adducts for illuminated U0 and U6.
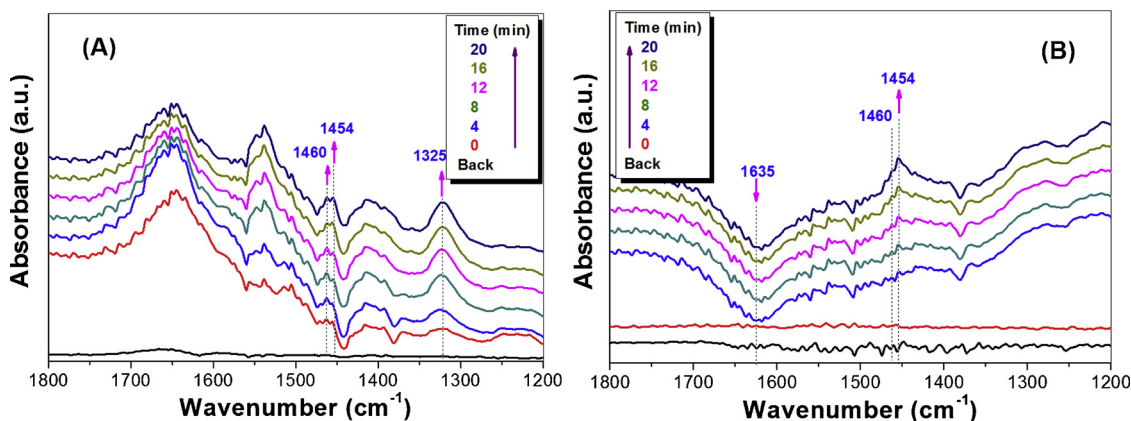

Fig. 14. Comparison of in situ FTIR spectra for NO adsorption on pristine TiO$_2$-HMSs (A) and Ov-TiO$_2$-HMSs (B).

all TiO$_2$-HMSs samples are similar (60–80 m^2 g^{-1}, see Table 1), the enhanced NO oxidation photoreactivity should be attributed to the introduction of Ov instead of the BET surface area. Note that Ov-TiO$_2$-HMSs is also very stable during the photocatalytic oxidation of NO. Its photoreactivity almost remains constant even after 8 times of recycling (Fig. 11), suggesting its promising practical application.

3.5. DFT calculations

To account for the increased NO oxidation efficiency of Ov-TiO$_2$, the adsorption of NO was simulated using DFT. It can be seen that the electronic local function of NO decreases from 0.82 (pristine TiO$_2$) to 0.78 (Ov-TiO$_2$), indicating that the N−O covalent bond is weakened by the stronger chemical adsorption on the surface of Ov-TiO$_2$-HMSs (Fig. 12A). The optimized structural models of NO adsorbed on the surface of pristine TiO$_2$ and Ov-TiO$_2$ are also compared (Fig. 12B). It can be clearly seen that the adsorption energy increases in magnitude from −0.10 eV (pristine TiO$_2$) to −0.29 eV (Ov-TiO$_2$), and the N−O bond length increases from 1.17 to 1.40 Å. These results suggest that the introduction of Ov facilitates the adsorption and activation of NO on the surface of TiO$_2$-HMSs, resulting in a weakened N−O bond. In addition, the Bader electron increases from 0.03 e (pristine TiO$_2$) to 1.06 e (Ov-TiO$_2$), indicating the preferential electron transfer from Ov to the adsorbed NO, which can enhance its photocatalytic activity.

Similar results are also obtained for the enhanced adsorption and activation of O$_2$ on the surface of TiO$_2$-HMSs after introduction of Ov (see Fig. S4). O$_2$ activation on the surface of Ov-TiO$_2$-HMSs is further confirmed by the increased concentration of reactive oxygen species (ROSs). The hydroxyl radicals (Fig. 13A) and superoxide radicals (Fig. 13B) are considered the most important ROSs that are responsible for NO oxidation [38,39]. Therefore, it is not strange to observe the

positive effect of Ov on the enhanced photocatalytic activity of TiO$_2$-HMSs.

The photocatalytic oxidation of NO over Ov-TiO$_2$-HMSs is summarized as follows (Eqs. (2)–(7)). Under the attacks of ROSs such as ·O$_2^-$ and ·OH, NO is oxidized into NO$_2$ and even HNO$_3$ [37,40]. Fig. S5 shows NO$_2$ evolution curve as irradiation time.

$$Ov\text{-}TiO_2 + h\gamma \rightarrow e^- + h^+ \quad (2)$$

$$O_2 + e^- = ·O_2\text{-} \quad (3)$$

$$h^+ + H_2O = H^+ + ·OH \quad (4)$$

$$NO + ·O_2^- \rightarrow NO_3\text{-} \quad (5)$$

$$NO + 2·OH \rightarrow NO_2 + H_2O \quad (6)$$

$$NO_2 + ·OH \rightarrow NO_3^- + H^+ \quad (7)$$

3.6. In situ DRIFT analysis

The introduction of Ov not only enhances the oxidation rate of NO, but also changes its photocatalytic oxidation pathway. Before photocatalytic oxidation, the effect of Ov on the activation of the adsorbed NO was determined. Fig. 14A shows the in situ FTIR adsorption spectra of the mixture NO and O$_2$ gases over pristine TiO$_2$-HMSs, where the increased absorption peaks centering at 1460 and 1325 cm^{-1} are identified as monodentate and bidentate nitrates, respectively [41]. Coincidentally, an additional peak centering at 1454 cm^{-1} also emerges, which originates from the adsorbed monodentate nitrites [42]. Therefore, the adsorbed NO on the surface of pristine TiO$_2$ transforms into NO$_2^-$ and NO$_3^-$. However, fewer NO$_3^-$ species can be detected on the surface of Ov-TiO$_2$-HMSs after adsorption of NO, as shown in Fig. 14B.

It can instead be seen that the absorption peak for adsorbed monodentate nitrites steadily increases. Thus, NO mainly transforms into NO_2^- on Ov-TiO_2-HMSs, in contrast to the case with pristine TiO_2.

We also prepared Ov-TiO_2-HMSs by calcination the mixure of H_2TiO_3-HMSs and other precursors of g-C_3N_4 such as cyanamide, dicyanodiamide and melamine under other identical conditions. EPR characterization results confirmed the successful introduction of Ov onto the surface of TiO_2-HMSs (Fig. S6). The prepared Ov-TiO_2-HMSs also exhibit improved photocatalytic activity towards NO oxidation (Fig. S7). Therefore, we present a general method for the fabrication of high photoreactive TiO_2 with surface oxygen vacancy.

4. Conclusions

In summary, visible-light-responsive TiO_2-HMSs, an ideal model for photocatalytic air purification, was successfully prepared by simple calcination of the mixture of the TiO_2-HMSs precursor and urea to introduce Ov, the concentration of which can be easily tailored by adjusting the amount of urea. The visible-light photocatalytic activity of Ov-TiO_2-HMSs toward NO oxidation steadily increases with an increase in the Ov concentration. The introduction of Ov has profound effects on the photoreactivity of TiO_2-HMSs, which include (1) extended light-response range due to the narrower bandgap, (2) retarded recombination of photo-generated carriers, (3) enhanced adsorption and activation of NO and O_2 on the surface, and (4) altered oxidation pathway of NO. The present method of introduction of Ov into TiO_2 has the merits of simplicity and ease of scale-up. Moreover, the excellent stability of Ov-TiO_2-HMSs makes it a promising photocatalyst for practical air purification.

Acknowledgements

Appendix A. Supplementary data

Supplementary material related to this article can be found, in the online version, at doi:https://doi.org/10.1016/j.apcatb.2019.117860.

References

[1] C.M. Li, Y. Xu, W.G. Tu, G. Chen, R. Xu, Metal-free photocatalysts for various applications in energy conversion and environmental purification, Green Chem. 19 (2017) 882–899.

[2] C.M. Li, S.Y. Yu, X.X. Zhang, Y. Wang, C.B. Liu, G. Chen, H.J. Dong, Insight into photocatalytic activity, universality and mechanism of copper/chlorine surface dual-doped graphitic carbon nitride for degrading various organic pollutants in water, J. Colloid Interface Sci. 538 (2019) 462–473.

[3] Q. Han, B. Wang, J. Gao, Z.H. Cheng, Y. Zhao, Z.P. Zhang, L.T. Qu, Atomically thin mesoporous nanomesh of graphitic C_3N_4 for high-efficiency photocatalytic hydrogen evolution, ACS Nano 10 (2016) 2745–2751.

[4] C.M. Li, Y.H. Du, D.P. Wang, S.M. Yin, W.G. Tu, Z. Chen, M. Kraft, G. Chen, R. Xu, Unique P-Co-N surface bonding states constructed on g-C_3N_4 nanosheets for drastically enhanced photocatalytic activity of H_2 evolution, Adv. Funct. Mater. (2017) 1604328.

[5] J.S. Cheng, Z. Hu, K.L. Lv, X.F. Wu, Q. Li, Y.H. Li, X.F. Li, J. Sun, Drastic promoting the visible photoreactivity of layered carbon nitride by polymerization of dicyandiamide at high pressure, Appl. Catal. B 232 (2018) 330–339.

[6] Q. Li, T. Shi, X. Li, K.L. Lv, M. Li, F.L. Liu, H.Y. Li, M. Lei, Remarkable positive effect of Cd(OH)$_2$ on CdS semiconductor for visible light photocatalytic H_2 production, Appl. Catal. B 229 (2018) 8–14.

[7] R.W. Yang, J.H. Cai, K.L. Lv, X.F. Wu, W.G. Wang, Z.H. Xu, M. Li, Q. Li, W.Q. Xu, Fabrication of TiO_2 hollow microspheres assembly from nanosheets (TiO_2-HMSs-NSs) with enhanced photoelectric conversion efficiency in DSSCs and photocatalytic activity, Appl. Catal. B 210 (2017) 184–193.

[8] W.J. Wang, J.C. Yu, D.H. Xia, P.K. Wong, Y.C. Li, Graphene and g-C_3N_4 nanosheets cowrapped elemental α-sulfur as a novel metal-free Heterojunction photocatalyst for bacterial inactivation under visible-light, Environ. Sci. Technol. 47 (2013) 8724–8732.

[9] X.T. Shen, L.H. Zhu, N. Wang, L. Ye, H.Q. Tang, Molecular imprinting for removing highly toxic organic pollutants, Chem. Commun. 48 (2012) 788–798.

[10] C.M. Li, S.Y. Yu, H.N. Che, X.X. Zhang, J. Han, Y.L. Mao, Y. Wang, C.B. Liu, H.J. Dong, Fabrication of Z-scheme heterojunction by anchoring mesoporous γ-Fe_2O_3 nanospheres on g-C_3N_4 for degrading tetracycline hydrochloride in water, ACS Sustain. Chem. Eng. 6 (2018) 16437–16447.

[11] C.M. Li, G. Chen, J.X. Sun, J.C. Rao, Z.H. Han, Y.D. Hu, W.N. Xing, C.M. Zhang, Doping effect of phosphate in Bi_2WO_6 and universal improved photocatalytic activity for removing various pollutants in water, Appl. Catal. B 188 (2016) 39–47.

[12] C.M. Li, S.Y. Yu, H.J. Dong, C.B. Liu, H.J. Wu, H.N. Che, G. Chen, Z-scheme mesoporous photocatalyst constructed by modification of Sn_3O_4 nanoclusters on g-C_3N_4 nanosheets with improved photocatalytic performance and mechanism insight, Appl. Catal. B 238 (2018) 284–293.

[13] C.M. Li, S.Y. Yu, H.J. Dong, Y. Wang, H.J. Wu, X.X. Zhang, G. Chen, C.B. Liu, Mesoporous ferriferrous oxide nanoreactors modified on graphitic carbon nitride towards improvement of physical, photoelectrochemical properties and photocatalytic performance, J. Colloid Interface Sci. 531 (2018) 331–342.

[14] C.M. Li, S.Y. Yu, Y. Wang, J. Han, H.J. Dong, G. Chen, Fabrication, physicochemical properties and photocatalytic activity of $Ag_{0.68}V_2O_5$ hierarchical architecture assembled by ultrathin nanosheets, J. Taiwan Inst. Chem. Eng. 87 (2018) 272–280.

[15] T. Shi, Y.Y. Duan, K.L. Lv, Z. Hu, Q. Li, M. Li, X.F. Li, Photocatalytic oxidation of acetone over high thermally stable TiO_2 nanosheets with exposed (001) facets, Front. Chem. 6 (2018) 175.

[16] J. Schneider, M. Matsuoka, M. Takeuchi, J.L. Zhang, Y. Horiuchi, M. Anpo, D.W. Bahnemann, Understanding TiO_2 photocatalysis: mechanisms and materials, Chem. Rev. 114 (2014) 9919–9986.

[17] X.W. Lou, L.A. Archer, Z.C. Yang, Hollow micro-/nanostructures: synthesis and applications, Adv. Mater. 20 (2008) 3987–4019.

[18] X. Li, J.G. Yu, M. Jaroniec, Hierarchical photocatalysts, Chem. Soc. Rev. 45 (2016) 2603–2636.

[19] G. Liu, H.G. Yang, X.W. Wang, L. Cheng, J. Pan, G.Q. Lu, H.M. Cheng, Visible light responsive nitrogen doped anatase TiO_2 sheets with dominant {001} facets derived from TiN, J. Am. Chem. Soc. 131 (2009) 12868–12869.

[20] C.C. Li, T. Wang, Z.J. Zhao, W.M. Yang, J.F. Li, A. Li, Z.L. Yang, G.A. Ozin, J.L. Gong, Promoted fixation of molecular nitrogen with surface oxygen vacancies on plasmon-enhanced TiO_2 photoelectrodes, Angew. Chem. Int. Ed. 57 (2018) 5278–5282.

[21] Z.A. Huang, Q. Sun, K.L. Lv, Z.H. Zhang, M. Li, B. Li, Effect of contact interface between TiO_2 and g-C_3N_4 on the photoreactivity of g-C_3N_4/TiO_2 photocatalyst: (001) vs (101) facets of TiO_2, Appl. Catal. B 164 (2015) 420–427.

[22] H.G. Yang, C.H. Sun, S.Z. Qiao, J. Zou, G. Liu, S.C. Smith, H.M. Cheng, G.Q. Lu, Anatase TiO_2 single crystals with a large percentage of reactive facets, Nature 453 (2008) 638–641.

[23] X.B. Chen, L. Liu, P.Y. Yu, S.S. Mao, Increasing solar absorption for photocatalysis with black hydrogenated titanium dioxide nanocrystals, Science 331 (2011) 746–750.

[24] D.J. Zhou, X.Y. Xiong, Z. Cai, N.N. Han, Y. Jia, Q.X. Xie, X.X. Duan, T.H. Xie, X.L. Zheng, X.M. Sun, X. Duan, Flame-engraved nickel–iron layered double hydroxide nanosheets for boosting oxygen evolution reactivity, Small Methods (2018) 1800083.

[25] H. Li, J.G. Shi, K. Zhao, L.Z. Zhang, Sustainable molecular oxygen activation with oxygen vacancies on the {001} facets of BiOCl nanosheets under solar light, Nanoscale 6 (2014) 14168–14173.

[26] G.G. Zhang, G.S. Li, Z.A. Lan, H.L. Lin, A. Savateev, T. Heil, S. Zafeiratos, X.C. Wang, M. Antonietti, Optimizing optical absorption, exciton dissociation, and charge transfer of a polymeric carbon nitride with ultrahigh solar hydrogen production activity, Angew. Chem. Int. Ed. 56 (2017) 13445–13449.

[27] Y. Zhang, J.H. Cai, K.L. Lv, J. Sun, H.P. Ye, M. Li, Hydrogen peroxide assisted rapid synthesis of TiO_2 hollow microspheres with enhanced photocatalytic activity, Appl. Catal. B 147 (2014) 789–795.

[28] G. Kresse, J. Furthmiiller, Efficiency of ab-initio total energy calculations for metals and semiconductors using a plane-wave basis set, Comput. Mater. Sci. 6 (1996) 15–50.

[29] D.L. Liu, C.H. Wang, Y.F. Yu, B.H. Zhao, W.C. Wang, Y.H. Du, B. Zhang, Understanding the nature of ammonia treatment to synthesize oxygen vacancy-enriched transition metal oxides, Chemistry 5 (2019) 376–389.

[30] X.Q. An, C.Z. Hu, H.J. Liu, J.H. Qu, Oxygen vacancy mediated construction of anatase/brookite heterophase junctions for high-efficiency photocatalytic hydrogen evolution, J. Mater. Chem. A 5 (2017) 24989–24994.

[31] J.Z. Ma, H.M. Wu, Y.C. Liu, H. He, Photocatalytic removal of NOx over visible light responsive oxygen-deficient TiO_2, J. Phys. Chem. C 118 (2014) 7434–7441.

[32] Y.Y. Duan, L. Liang, K.L. Lv, Q. Li, M. Li, TiO_2 faceted nanocrystals on the nanofibers: homojunction TiO_2 based Z-scheme photocatalyst for air purification, Appl. Surf. Sci. 456 (2018) 817–826.

[33] H. Li, J. Li, Z.H. Ai, F.L. Jia, L.Z. Zhang, Oxygen vacancy-mediated photocatalysis of BiOCl: reactivity, selectivity, and perspectives, Angew. Chem. Int. Ed. 57 (2018) 122–138.

[34] J.C. Yu, J.G. Yu, W.K. Ho, Z.T. Jiang, L.Z. Zhang, Effects of F- doping on the photocatalytic activity and microstructures of nanocrystalline TiO_2 powders, Chem. Mater. 14 (2002) 3808–3816.

[35] Y.H. Li, X.F. Wu, W.K. Ho, K.L. Lv, Q. Li, M. Li, S.C. Lee, Graphene-induced formation of visible-light-responsive SnO_2-Zn_2SnO_4 Z-scheme photocatalyst with surface vacancy for the enhanced photoreactivity towards NO and acetone oxidation, Chem. Eng. J. 336 (2018) 200–210.

[36] K.L. Lv, J.C. Hu, X.H. Li, M. Li, Cysteine modified anatase TiO_2 hollow microspheres with enhanced visible-light-driven photocatalytic activity, J. Mol. Catal. A 356

(2012) 78–84.

[37] F. Dong, Z.Y. Wang, Y.H. Li, W.K. Ho, S.C. Lee, Immobilization of polymeric g-C$_3$N$_4$ on structured ceramic foam for efficient visible light photocatalytic air purification with real indoor illumination, Environ. Sci. Technol. 48 (2014) 10345–10353.

[38] L. Zhang, C. Yang, K.L. Lv, Y.C. Lu, Q. Li, X.F. Wu, Y.H. Li, X.F. Li, J.J. Fan, M. Li, SPR effect of bismuth enhanced visible photoreactivity of Bi$_2$WO$_6$ for NO abatement, Chin. J. Catal. 40 (2019) 755–764.

[39] X.F. Wu, J.S. Cheng, X.F. Li, Y.H. Li, K.L. Lv, Enhanced visible photocatalytic oxidation of NO by repeated calcination of g-C$_3$N$_4$, Appl. Surf. Sci. 456 (2019) 1037–1046.

[40] F. Dong, Z.W. Zhao, Y.J. Sun, Y.X. Zhang, S. Yan, Z.B. Wu, An advanced semimetal-organic Bi spheres-g-C$_3$N$_4$ nanohybrid with SPR-enhanced visible-light photocatalytic performance for NO purification, Environ. Sci. Technol. 49 (2015) 12432–12440.

[41] T. Ohno, F. Hatayama, Y. Toda, S. Konishi, H. Miyata, Fourier transform infrared studies of reduction of nitric oxide by ethylene over V$_2$O$_5$ layered on ZrO$_2$, Appl. Catal. B 5 (1994) 89–101.

[42] L.D. Li, Q. shen, J. Cheng, Z.P. Hao, Catalytic oxidation of NO over TiO$_2$ supported platinum clusters. II: mechanism study by in situ FTIR spectra, Catal. Today 158 (2010) 361–369.